The Astrophysical Journal, 977:203 (12pp), 2024 December 20 https://doi.org/10.3847/1538-4357/ad90b3

Massive Star Cluster Formation with Binaries. I. Evolution of Binary Populations

Claude Cournoyer-Cloutier[1], Alison Sills[1], William E. Harris[1], Brooke Polak[2,3], Steven Rieder[4,5], Eric P. Andersson[3], Sabrina M. Appel[3,6,9], Mordecai-Mark Mac Low[3], Stephen McMillan[7], and Simon Portegies Zwart[8]
[1] Department of Physics and Astronomy, McMaster University, 1280 Main Street West, Hamilton, ON, L8S 4M1, Canada; cournoyc@mcmaster.ca
[2] Zentrum für Astronomie, Institut für Theoretische Astrophysik, Universität Heidelberg, Albert-Ueberle-Str. 2, 69120 Heidelberg, Germany
[3] Department of Astrophysics, American Museum of Natural History, 200 Central Park West, New York, NY 10024-5102, USA
[4] Anton Pannekoek Institute for Astronomy, University of Amsterdam, Science Park 904, 1098 XH Amsterdam, The Netherlands
[5] Institute of Astronomy, Department of Phyiscs and Astronomy, KU Leuven, Celestijnenlaan 200D bus 2401, 3001 Leuven, Belgium
[6] Department of Physics and Astronomy, Rutgers University, 136 Frelinghuysen Road, Piscataway, NJ 08854-8019, USA
[7] Department of Physics, Drexel University, 3141 Chestnut Street, Philadelphia, PA 19104, USA
[8] Sterrewacht Leiden, Leiden University, Einsteinweg 55, 2333CC Leiden, The Netherlands

Received 2024 October 9; revised 2024 November 7; accepted 2024 November 8; published 2024 December 13

Abstract

We study the evolution of populations of binary stars within massive cluster-forming regions. We simulate the formation of young massive star clusters within giant molecular clouds with masses ranging from 2×10^4 to $3.2 \times 10^5\,M_\odot$. We use TORCH, which couples stellar dynamics, magnetohydrodynamics, star and binary formation, stellar evolution, and stellar feedback through the AMUSE framework. We find that the binary fraction decreases during cluster formation at all molecular cloud masses. The binaries' orbital properties also change, with stronger and quicker changes in denser, more massive clouds. Most of the changes we see can be attributed to the disruption of binaries wider than 100 au, although the close binary fraction also decreases in the densest cluster-forming region. The binary fraction for O stars remains above 90%, but exchanges and dynamical hardening are ubiquitous, indicating that O stars undergo frequent few-body interactions early during the cluster formation process. Changes to the populations of binaries are a by-product of hierarchical cluster assembly: most changes to the binary population take place when the star formation rate is high, and there are frequent mergers between subclusters in the cluster-forming region. A universal primordial binary distribution based on observed inner companions in the Galactic field is consistent with the binary populations of young clusters with resolved stellar populations, and the scatter between clusters of similar masses could be explained by differences in their formation history.

Unified Astronomy Thesaurus concepts: Young massive clusters (2049); Young star clusters (1833); Star clusters (1567); Star forming regions (1565); Star formation (1569); Binary stars (154)

1. Introduction

Young massive clusters (YMCs) are ubiquitous in nearby star-forming galaxies, with populations of massive clusters embedded in their natal gas observed in nearby starbursts (e.g., H. He et al. 2022; J. Sun et al. 2024). Observations have also found massive and compact star clusters at high redshift (e.g., $z \sim 6$, E. Vanzella et al. 2023; $z \sim 10.2$, A. Adamo et al. 2024), and globular clusters (GCs) at $z = 1.38$ (e.g., A. Adamo et al. 2023; A. Claeyssens et al. 2023) and at $z \sim 0.3$–0.4 (e.g., A. L. Faisst et al. 2022; M. G. Lee et al. 2022; W. E. Harris & M. Reina-Campos 2023). These observations serve as growing evidence that GC formation is the extension at high masses of YMC formation in the local Universe. This is also supported by simulations, which have shown that star clusters of masses $\gtrsim 10^6\,M_\odot$ form naturally within massive giant molecular clouds (GMCs; e.g., C. S. Howard et al. 2018; B. Polak et al. 2024a; M. Reina-Campos et al. 2024). Detailed analysis of the stellar populations of YMCs and GMCs within which they form is limited to the Milky Way and the LMC/SMC, for which the cluster mass function does not reach the high masses observed in starbursts (S. F. Portegies Zwart et al. 2010). This is a challenge for understanding the spatial and kinematic properties of the stars, including the binary fraction, which is largely unknown for the most massive YMCs.

Massive stars, which regulate star formation within their host cluster, have binary fractions approaching unity (M. Moe & R. Di Stefano 2017), and two-thirds of all massive stars exchange material with a companion over their lifetimes (H. Sana et al. 2012). This changes the time distribution of supernovae (E. Zapartas et al. 2017), increases the amount of ultraviolet radiation (Y. Götberg et al. 2018), and increases the amount of pre-supernova ejecta from a stellar population by a factor of ∼6 (M. Nguyen & A. Sills 2024). Binaries can produce runaway stars either through the ejection of a newly unbound companion after a supernova (A. Blaauw 1961) or through few-body interactions (A. Poveda et al. 1967). Such runaway stars are known to be ubiquitous around young clusters (e.g., V. M. Kalari et al. 2019; M. Stoop et al. 2023, 2024), and in turn, influence the distribution of feedback within cluster-forming regions, which can affect the long-term evolution of galaxies (E. P. Andersson et al. 2020, 2023; U. P. Steinwandel et al. 2023).

Clustered environments also influence the binaries found within them: high stellar densities promote few-body interactions that can result in the formation, modification, or disruption of binaries. Observationally, surveys of binaries in clustered environments suggest a dependence of the binary fraction and orbital properties of binaries on cluster density and/or cluster mass. The frequency and orbital properties of

---

[9] NSF Astronomy and Astrophysics Postdoctoral Fellow

close (<10 au) companions to low- and solar-mass stars appear to be set very early in the stars' evolution (e.g., M. Kounkel et al. 2019) and to persist both in young open clusters (e.g., N. R. Deacon & A. L. Kraus 2020) and in the field, suggesting that the field properties observed for those systems resemble the primordial ones. On the other hand, the wide binary fraction depends on environment: low-density star-forming regions show an excess of wide companions (e.g., Taurus, A. L. Kraus et al. 2011; I. Joncour et al. 2017), while high-density star-forming regions show fewer wide companions (e.g., Orion, G. Duchêne et al. 2018; T. Jerabkova et al. 2019). It has been suggested that the binary fraction observed in the field arises from a combination of binary fractions inherited from stars formed in embedded clusters of varying densities, which have since dissolved (see S. S. R. Offner et al. 2023, for a discussion). Observations of older clusters do not fully support this picture. For open clusters, surveys have found evidence of binary fraction either increasing (e.g., H. Niu et al. 2020) or decreasing (N. R. Deacon & A. L. Kraus 2020) with stellar density, depending on which clusters were observed and what separation range was probed. The older, denser, more massive GCs consistently show low binary fractions, which are anticorrelated with cluster mass but do not, however, show any trends with cluster density (e.g., A. P. Milone et al. 2012). Taken together, these results indicate that there is more at play than just the present-day densities for setting the binary fraction and binary properties.

We need to understand how a binary population evolves during the formation of clusters at a range of masses and densities in order to fully understand cluster formation and long-term evolution. Numerical simulations provide us with detailed spatial and kinematic information about each star within a YMC as a function of time. Modeling the stars alongside gas, which is affected by feedback, is crucial: populations of binaries are modified during cluster assembly (C. Cournoyer-Cloutier et al. 2021), and these changes are driven by subcluster mergers (C. Cournoyer-Cloutier et al. 2024), which are in turn dependent on the GMC-scale gas environment (N. Lahén et al. 2020; D. Guszejnov et al. 2022; J. Karam & A. Sills 2024).

We present a suite of simulations with cloud masses ranging from 2×10^4 to $3.2 \times 10^5\, M_\odot$ to test the dependence of binary properties on environment during star cluster formation. Those simulations include primordial binaries, star formation, and stellar feedback, along with collisional stellar dynamics and magnetohydrodynamics (MHD). We describe our simulation methods in Section 2 and our suite of simulations in Section 3. We present our results in Section 4 and discuss their implications for globular cluster formation in Section 5. We conclude in Section 6.

2. Methods

We perform our simulations with TORCH[10] (J. E. Wall et al. 2019, 2020), which couples MHD to star formation, stellar dynamics, stellar evolution, and stellar feedback through the AMUSE framework (S. Portegies Zwart et al. 2009; F. I. Pelupessy et al. 2013; S. F. Portegies Zwart et al. 2013; S. Portegies Zwart & S. L. W. McMillan 2019). The coupling between the different codes is presented in J. E. Wall et al. (2019). The physics in our simulations are described in more detail in the following sections. Parameters for star formation, feedback, *N*-body dynamics, and binary formation, which are shared between the simulations, are summarized in Table 1.

Table 1
Parameters for the Simulations

	Definition	Value
$\Delta x_{\rm min}$	Minimum cell size	0.137 pc
$r_{\rm sink}$	Sink particle accretion radius	0.342 pc
$\rho_{\rm sink}$	Gas density for sink formation	$93.5\ M_\odot\ {\rm pc}^{-3}$
$M_{\rm sink}$	Minimum sink mass at formation	$3.74\ M_\odot$
$T_{\rm wind}$	Wind target temperature	3×10^5 K
$r_{\rm out}$	Changeover radius for FDPS	Section 2.2
$r_{\rm in}$	Changeover radius for *N*-body	$0.1\ r_{\rm out}$
$r_{\rm bin}$	Changeover radius for SDAR	100 au
$M_{\rm min}$	Minimum stellar mass	$0.4\ M_\odot$
$M_{\rm max}$	Maximum stellar mass	$150\ M_\odot$
$M_{\rm FB}$	Minimum mass for feedback	$13\ M_\odot$
$\mathcal{F}_{\rm bin}$	Binary fraction	Section 2.4

Note. $r_{\rm out}$ depends on the simulation time step and is described in Section 2.2. $\mathcal{F}_{\rm bin}$ depends on the stellar mass and is described in Section 2.4.

2.1. MHD

We use FLASH (B. Fryxell et al. 2000; A. Dubey et al. 2014) with a Harten–Lax–van Leer Riemann solver (T. Miyoshi & K. Kusano 2005) with third-order piecewise parabolic method reconstruction (P. Colella & P. R. Woodward 1984). We use a multigrid solver (P. M. Ricker 2008) for the gas self-gravity. Gravity between the gas and stars is treated with a leapfrog scheme based on BRIDGE (M. Fujii et al. 2007). We refine our adaptive grid such that the Jeans length is resolved by at least 12 resolution elements to ensure that it can be magnetically supported against collapse on scales below the resolution (F. Heitsch et al. 2001, see also the discussion in C. Federrath et al. 2010). To improve numerical stability in regions with large temperature or pressure gradients, such as H II regions, we also refine where the second derivative of the temperature or pressure is of the order of the sum of its gradients (see R. Lohner 1987; P. MacNeice et al. 2000). Sink particles are used to model subgrid star and binary formation. Sinks form in regions of high gas density and converging flows, which satisfy the boundedness and gravitational instability criteria outlined in C. Federrath et al. (2010). The sink accretion radius is set to $2.5\Delta x$ at the highest refinement level, and sinks can only form in regions that are refined to the highest refinement level. We give more details on the formation of stars from sinks in Section 2.5.

2.2. Stellar Dynamics

We handle stellar dynamics, including hard binaries and close encounters, with the *N*-body code PETAR (L. Wang et al. 2020a, see B. Polak et al. 2024a for the implementation in TORCH). PETAR relies on a combination of three different *N*-body algorithms: long-range interactions are calculated with a Barnes–Hut tree (J. Barnes & P. Hut 1986, as implemented in FDPS by M. Iwasawa et al. 2016), short-range interactions are calculated with a fourth-order Hermite integrator (J. Makino &

---

[10] https://bitbucket.org/torch-sf/torch/src/binaries-v2.0/

S. J. Aarseth 1992), and binary systems and few-body encounters are calculated with the slow-down algorithmic regularization (SDAR) method (L. Wang et al. 2020b).

The changeover radii between these three integration regimes are set by the user. The default values calculated by PETAR are optimized for a spherical stellar system with a fixed number of stars. However, our cluster-forming regions continuously form new stars, and are not well described by a single spherical cluster at early times. They also span a range of densities. As we are interested in the evolution of binaries within these fast-changing stellar systems, we adopt larger changeover radii than previous work using PETAR: this is less efficient than optimizing PETAR for binaries expected to survive the cluster's long-term evolution, but ensures that we fully capture the complexity of stellar dynamics within the cluster-forming region. Binary systems on scales smaller than $r_{\rm bin}$ are treated by SDAR, ensuring that they do not affect the global time step of the simulation. Forces between stars closer than $r_{\rm in}$ are calculated using the fourth-order Hermite, forces between stars more distant than $r_{\rm out}$ are calculated using the Barnes–Hut tree, and forces between stars with separations between $r_{\rm in}$ and $r_{\rm out}$ are treated using a combination of the Hermite and tree codes.

The changeover radius for SDAR $r_{\rm bin}$ is kept fixed in our simulations. We adopt a value of 100 au as this corresponds to an orbital period of 58 yr for a binary with two stars of mass $150\,M_\odot$ (the largest stellar mass in our simulations). As a typical time step for our simulations is between 15.625 yr and 62.5 yr, this ensures that the orbits of massive binaries (with large orbital velocities) are well resolved in our simulations. 100 au is also commonly used as the lower semimajor axis limit for wide binaries in observational surveys (see S. S. R. Offner et al. 2023, and references therein).

The changeover radii $r_{\rm in}$ and $r_{\rm out}$ have a strong impact on the performance of the code but must be chosen carefully in conjunction with the simulation time step to ensure that the orbits of binaries wider than 100 au but still strongly bound are well resolved. TORCH uses a single time step for MHD and stellar dynamics; as we model star-forming regions with shock fronts and high sound speeds, the time step calculated by FLASH decreases drastically after the formation of the first massive star. On the other hand, the PETAR time step must always remain a power of 2 of the initial PETAR time step, which we set to 1000 yr. The only allowed time steps for the simulation are therefore

$$\Delta t = \frac{1000}{2^n}\ \mathrm{yr} \tag{1}$$

where n is a positive integer. After the formation of the first star, we set the maximum time step and $r_{\rm out}$ together, such that the orbit of a circular binary with a semimajor axis of $r_{\rm out}$ is resolved by 10 time steps if the two stars have a mass of $10\,M_\odot$. For our simulations, the shortest minimum time step used is 7.8125 yr and the longest minimum time step used is 125 yr, which correspond, respectively, to $r_{\rm out} = 0.00112$ pc and $r_{\rm out} = 0.00709$ pc. The inner changeover radius $r_{\rm in}$ is set to $0.1\ r_{\rm out}$ at all times, following the standard approach in PETAR. The computational time is insensitive to our choice of PETAR time step, as the computational time per time step is dominated by FLASH for all time steps used in the paper.

2.3. Initial Mass Function Sampling

Star formation takes place via sink particles from which individual stars are spawned. This process is described in detail in J. E. Wall et al. (2019) and the modifications to this method to allow for primordial binary formation are described in C. Cournoyer-Cloutier et al. (2021). As each sink is formed, we sample a P. Kroupa (2002) initial mass function (IMF) and apply a primordial binary prescription, described in Section 2.4, to generate a list of stars to be formed. We use a lower limit of $0.4\,M_\odot$ and an upper limit of $150\,M_\odot$ to sample the IMF. The lower limit reduces the number of stars by a factor of 2 compared to sampling down to $0.08\,M_\odot$, reducing the load on the N-body integrator while retaining 90% of the stellar mass in stars of the mass predicted by the IMF. Each sampled star corresponds to a star particle to ensure that the shape of the IMF is preserved. Although low-mass binaries are important to the long-term evolution of star clusters once massive stars have evolved, they are not the leading source of binding energy in young cluster-forming regions, which host several massive stars for which the close binary fraction approaches unity. We inject radiative and wind feedback from all stars more massive than $13\,M_\odot$.

2.4. Primordial Binaries

We use the module for primordial binaries in TORCH that was first presented in C. Cournoyer-Cloutier et al. (2021), in which we implement an updated sampling binary algorithm. We use a mass-dependent binary fraction based on observations made by J. G. Winters et al. (2019) and corrected by S. S. R. Offner et al. (2023) for stars below $0.6\,M_\odot$, and on observations compiled by M. Moe & R. Di Stefano (2017) for stars above $0.8\,M_\odot$; the only difference between those fractions and those used in C. Cournoyer-Cloutier et al. (2021) is the correction by S. S. R. Offner et al. (2023) of the binary fraction for $M \leqslant 0.6\,M_\odot$. The sampling technique for the orbital period, companion mass, and eccentricity also remains the same as in C. Cournoyer-Cloutier et al. (2021).

The key change in the updated sampling algorithm is in the distribution of orbital periods. The sampling algorithm used in C. Cournoyer-Cloutier et al. (2021) sampled any companion from a distribution of observed properties, while the new algorithm presented here is designed to sample the inner companion of a hierarchical multiple stellar system. The triple fraction ranges from 10% for solar-mass stars to 73% for O-type stars (M. Moe & R. Di Stefano 2017), which implies that the distribution of *all companions* to O stars is quite different from the distribution of *inner companions* to O stars. The updated algorithm therefore accounts for the dynamical formation of hierarchical triples and higher-order multiples while preserving the observed close binary fraction. For stars with masses above $0.8\,M_\odot$, we impose that a fraction $\mathcal{F}_{\rm close}$ of all stars in each mass range must have a companion with an orbital period shorter than 5000 days. For a binary of total mass $100\,M_\odot$, this corresponds to a semimajor axis of roughly 27 au, while it corresponds to a semimajor axis of about 10 au for a binary with total mass $5\,M_\odot$. For stars with masses below $0.8\,M_\odot$, we use the lognormal distribution of semimajor axes for inner companions from J. G. Winters et al. (2019), as reported and corrected in S. S. R. Offner et al. (2023), which corresponds to a mean semimajor axis of 14 au for close binaries. A fraction $\mathcal{F}_{\rm bin} - \mathcal{F}_{\rm close}$ of stars in each mass bin will

Table 2
Binary Fraction, Close Binary Fraction, Median Semimajor Axis, and Median Mass Ratio for Each Mass Range

Mass Range	$\mathcal{F}_{\rm bin}$	$\mathcal{F}_{\rm close}$	$a_{\rm median}$	$q_{\rm median}$
0.4–0.8 $M_\odot$	0.30	0.07	44.6 au	0.90
0.8–1.6 $M_\odot$	0.40	0.15	201 au	0.67
1.6–5 $M_\odot$	0.59	0.37	21.6 au	0.41
5–9 $M_\odot$	0.76	0.63	9.92 au	0.34
9–16 $M_\odot$	0.84	0.80	7.08 au	0.35
$\geqslant$16 $M_\odot$	0.94	0.94	6.72 au	0.37

Note. Those values are calculated for a fully sampled distribution of binaries.

have a companion with an orbital period longer than 5000 days. The binary fraction, close binary fraction, median semimajor axis, and median mass ratio for each mass bin are reported in Table 2.

The sampling algorithm only forms systems that do not fill their Roche lobe while on the zero-age main sequence. This is done using an upper limit on the eccentricity as a function of period based on the semi-analytic formula from M. Moe & R. Di Stefano (2017), as described in C. Cournoyer-Cloutier et al. (2021),

$$e_{\max}(P) = \left(\frac{P}{2\ \mathrm{days}}\right)^{-2/3} \tag{2}$$

where P is the orbital period in days. Stars are allowed to merge during the simulations, but other binary evolution effects—such as stable or unstable mass transfer—are not taken into account.

2.5. Feedback

Radiation from stars more massive than 13 $M_\odot$ is followed using the ray-tracing scheme Fervent (C. Baczynski et al. 2015), which follows radiation pressure in the far-ultraviolet (band (5.6–13.6 eV) and ionizing radiation (above 13.6 eV) from individual massive stars. Momentum-driven winds are also injected into the grid by massive stars. The implementation of both forms of feedback is described in J. E. Wall et al. (2020). Torch also includes a scheme for core-collapse supernovae, implemented within Flash; our simulations, however, stop before any supernovae take place. We mass load our winds by increasing the wind mass loss rate $\dot{M}$ while keeping the wind luminosity L_w fixed, therefore lowering the wind velocity v_w, following

$$L_w = \frac{1}{2}\dot{M}v_w^2. \tag{3}$$

The wind velocity is reduced to reach a target post-shock wind temperature

$$T_w = 1.38 \times 10^7\ \mathrm{K}\left(\frac{v_w}{10^3\ \mathrm{km\ s^{-1}}}\right)^2 \tag{4}$$

following J. E. Wall et al. (2020). We mass load the winds to a target temperature $T_w = 3 \times 10^5$ K, which was shown to be a reasonable choice in B. Polak et al. (2024a) and allows for a longer time step. Mass loading makes the wind bubbles momentum-driven rather than energy-driven. Momentum-driven winds are naturally produced by high-resolution hydrodynamics wind simulations (see, e.g., L. Lancaster et al. 2021): mass loading our winds allows us to reproduce the effects of the winds on cluster scale at the resolution of our simulations.

3. Overview of Simulations

3.1. Initial Conditions

We run a suite of isolated cloud simulations with initial gas masses of 2×10^4, 8×10^4, and $3.2 \times 10^5\ M_\odot$ and an initial cloud radius $R = 7$ pc. Each model is run for at least 2.5 freefall times (calculated for the initial cloud), with the lowest mass model run until gas expulsion. As GMC masses correlate with GMC surface densities but show little to no correlation with GMC radius or virial parameter for extragalactic GMCs (J. Sun et al. 2022), we vary the initial GMC mass but keep the radius fixed, which changes the surface density and the density between simulations. The surface densities for M1, M2, and M3 are chosen, respectively, to mimic GMC conditions typical of the disk of the Milky Way (e.g., J. Roman-Duval et al. 2010; B.-Q. Chen et al. 2020), the Central Molecular Zone or centers of barred galaxies (e.g., J. Sun et al. 2020), and starburst galaxies (e.g., J. Sun et al. 2018). All simulation domains have a box side of $L = 2.5R = 17.5$ pc. All models are initialized with an initial virial parameter $\alpha = 2T/|U| = 0.5$, a Kolmogorov turbulent velocity spectrum with the same random seed, and a uniform magnetic field $B_z = 3\ \mu G$. The initial GMCs are isolated, and the simulations do not include any external tidal field, which would not affect the clusters' evolution on the short (<5 Myr) timescales considered (see M. Miholics et al. 2017). The initial conditions are summarized in Table 3. The gas column density overlaid with the stellar distribution is presented in Figure 1 for all simulations, shown at the same fractions of their respective initial freefall times.

3.2. Star Formation

We summarize the key star formation metrics in Table 3, and plot the star formation rate (SFR) as a function of time in Figure 2. As expected, the star formation rate increases with initial gas mass, but in excess of the increase in mass—in other words, the increased total gas mass results in more stars formed, but the increased initial surface density also increases both the SFR and the star formation efficiency (SFE). In M1 and M2, the star formation rate peaks after roughly 1.6 $t_{\rm ff}$, and plateaus for the next freefall time. On the other hand, in M3, the SFR continues to increase beyond $\sim$1.5 $t_{\rm ff}$, and is still increasing at $\sim$2.5 $t_{\rm ff}$. The high initial gas mass and surface density (>$10^3\ M_\odot\ \mathrm{pc}^{-2}$) prevent the feedback from efficiently stopping star formation (see the discussion in S. H. Menon et al. 2023; B. Polak et al. 2024a). We also verify what mass fraction of the stars is bound at 2.5 $t_{\rm ff}$, and find a bound mass fraction above 98% for all three simulations. We note that the differences in SFE lead to a super-linear relation between bound stellar mass and initial cloud mass, which allows us to probe a larger range of stellar masses within a cluster-forming region than suggested by the mass range of our initial clouds.

3.3. Stellar Density

The differences in SFR and SFE have consequences for the density of the subclusters embedded within the GMC. Due to the high degree of substructure and nonsphericity of the systems, rather than calculating a global measure of density, we

Table 3
Initial Conditions and Star Formation Metrics for the Simulations

Cloud (1)	$M_{\rm gas}$ ($M_\odot$) (2)	R (pc) (3)	Σ ($M_\odot$ pc^{-2}) (4)	$t_{\rm ff}$ (Myr) (5)	SFE (2.5 $t_{\rm ff}$) (6)	$F_{\rm bound}$ (2.5 $t_{\rm ff}$) (7)	SFE (8)	$M_{\rm formed}$ ($M_\odot$) (9)	$t_{\rm SFR}$ (10)
M1	2×10^4	7	130	1.06	0.33	0.98	0.39	7.8×10^3	1.56
M2	8×10^4	7	520	0.530	0.40	0.99	$\geqslant$0.43	3.44×10^4	1.64
M3	3.2×10^5	7	2080	0.265	0.61	0.99	$\geqslant$0.61	1.95×10^5	$\gtrsim$2.46

Note. Column (1): cloud label. Column (2): initial mass. Column (3): initial radius. Column (4): initial surface density. Column (5): initial freefall time of the gas cloud. Column (6): SFE after 2.5 $t_{\rm ff}$. Column (7): bound mass fraction after 2.5 $t_{\rm ff}$. Column (8): total star SFE. Column (9): formed stellar mass. Column (10): time at which the SFR peaks (in units of freefall times).

adopt a local measure of stellar density. We calculate the local stellar density based on the distance to stars' nearest neighbors and their masses, using

$$\rho = \frac{3}{4\pi r_{10}^3}\sum_{i=1}^{10} m_i \qquad (5)$$

where m_i is the mass of the ith nearest neighbor and r_{10} is the radial distance to the 10th nearest neighbor, where the star itself is defined as its own closest neighbor. We plot the median and 90th percentile local stellar densities in Figure 3.

For M1, the distribution of local densities shifts to higher values while the SFR is increasing and during its plateau. However, once star formation has slowed, the local densities start decreasing, with the median approaching 50 $M_\odot$ pc^{-3} at late times. At all times, the stars in the highest density regions have local densities above 10^4 $M_\odot$ pc^{-3} (with more than 10% of all stars in environments with local density $>10^4$ $M_\odot$ pc^{-3} between 1.5 and 2 $t_{\rm ff}$), which is a density typical of local YMCs (S. F. Portegies Zwart et al. 2010, and references therein). The distribution of local stellar densities even extends to 10^5 $M_\odot$ pc^{-3} at early times. M2 follows similar trends but at higher densities. The decrease in densities also takes place at later times, following the longer plateau in the SFR. M3, on the other hand, exhibits very high densities: at late times, the median local density is above 10^5 $M_\odot$ pc^{-3}, and more than 10% of stars have local densities above 10^6 $M_\odot$ pc^{-3}. This environment promotes few-body interactions and is likely to lead to binary disruption, runaway star production, and stellar mergers. The difference in the local density in the different cluster-forming regions demonstrates that we are probing different regimes for cluster formation with our models at different initial gas masses. Although there is only a factor of 16 difference in the initial gas mass between M1 and M3, the median local stellar density after ∼2.5 $t_{\rm ff}$ differs by more than 2 orders of magnitude.

4. Evolution of Binary Populations

Between any two consecutive snapshots, several effects modify the number and properties of the binaries: there is ongoing primordial binary formation (adding new systems sampled from the primordial distribution) combined with dynamical binary formation, disruption, and modification (through exchanges or encounters changing the orbital energy). In this section, we study the relative contributions of those processes to the binary population present in the cluster-forming region as a function of time. In Sections 4.1 and 4.2, we discuss how the binary fraction and the orbital properties evolve with time. In Section 4.3, we discuss how exchanges and dynamical binary formation contribute to observed changes in the distribution, while we discuss the influence of environment in Section 4.4.

4.1. Time Evolution of Binary Fraction

We plot the binary fraction as a function of time in Figure 4. We find that the binary fraction decreases with time in all models. Most of the decrease can be attributed to the loss of binaries wider than 100 au: all three simulations show a clear decrease in their wide binary fraction. The most massive model, M3, is the only cluster-forming region that also shows a decrease in its close binary fraction, most likely due to the very high stellar densities it reaches.

1. For M1, which stops forming stars around 3.5 $t_{\rm ff}$, most of the decrease takes place between ∼1.5 and 2 $t_{\rm ff}$, while the star formation rate is high and the stellar density is increasing. At early times, the number of stars is too small to fully sample the binary population. At late times, once star formation has stopped, the binary fraction shows no significant evolution.
2. In M2, the binary fraction generally decreases, but reaches a small plateau after roughly 1.5 $t_{\rm ff}$—this corresponds to a peak in the star formation, during which the formation of new primordial binaries balances out the dynamical disruption of wide binaries.
3. The decrease in the binary fraction is most obvious, and most rapid, in M3. Both M2 and M3 have binary fractions higher than the primordial binary fraction at early times (before ∼ 1.5 $t_{\rm ff}$), due to the dynamical formation of wide binaries that are disrupted at later times.

4.2. Time Evolution of Orbital Properties

In this section, we use M3 as our example for the plots: it contains enough stars to fully sample the IMF and distribution of binary properties, and it exhibits the strongest signatures of the evolution of its binary population due to its high density. We do, however, note that all trends discussed below are found in all three cluster-forming regions.

4.2.1. Semimajor Axis

We plot the probability distribution function (PDF) of semimajor axes for M3 at different times in Figure 5 (top left), with the primordial distribution shown in black, accompanied by the distribution normalized to the primordial distribution (top right). The distribution of semimajor axes shifts toward smaller values with time. The largest changes in the distribution

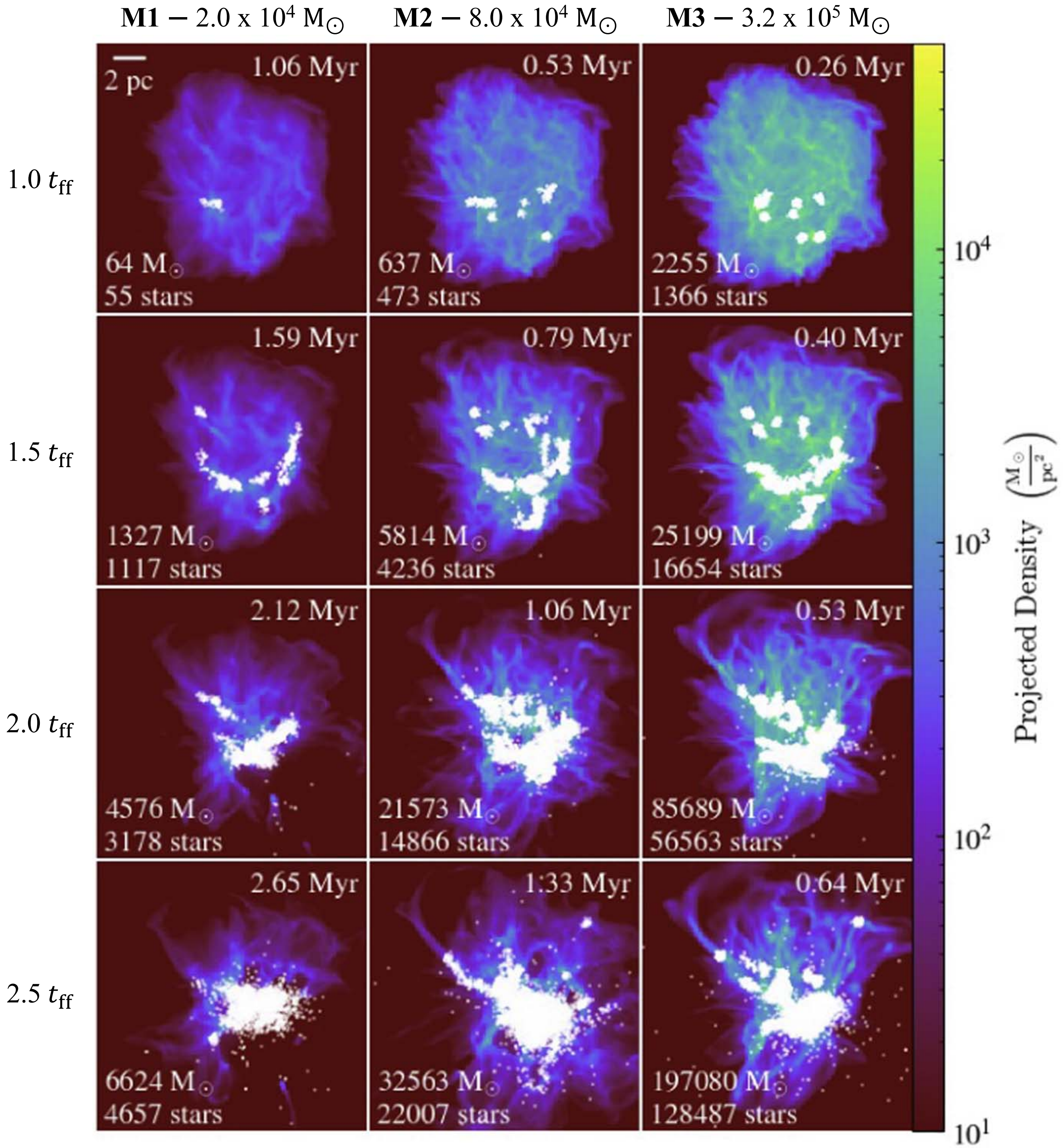

Figure 1. Gas column density, with stars overplotted as small white circles. The columns correspond to the different simulations, while the rows show the distribution of stars and gas at approximately 1.0, 1.5, 2.0, and 2.5 freefall times of the initial GMC.

are found when the star formation rate is high and the local stellar density is increasing, between 1.5 and 2.5 t_{ff}. Before ∼1.5 t_{ff}, there is a peak at wide separations, associated with dynamically formed systems. This effect is more obvious before the distribution of primordial binaries is fully sampled (∼1 t_{ff} for M3). Beyond ∼1.5 t_{ff}, the fraction of binary systems with separations above 100 au tends to decrease. The fraction of binaries with smaller separations increases, with a stronger increase for systems with semimajor axes below 10 au. Taken together with the results presented in Figure 4, this indicates that the overall fraction of stars with at least one bound companion decreases, as well as the fraction of stars with a companion within 100 au; among stars with a bound companion, however, the fraction of bound companions within 100 au increases.

4.2.2. Primary Mass and Mass Ratio

We plot the PDF of primary masses and mass ratios (normalized to the primordial distribution) as a function of time

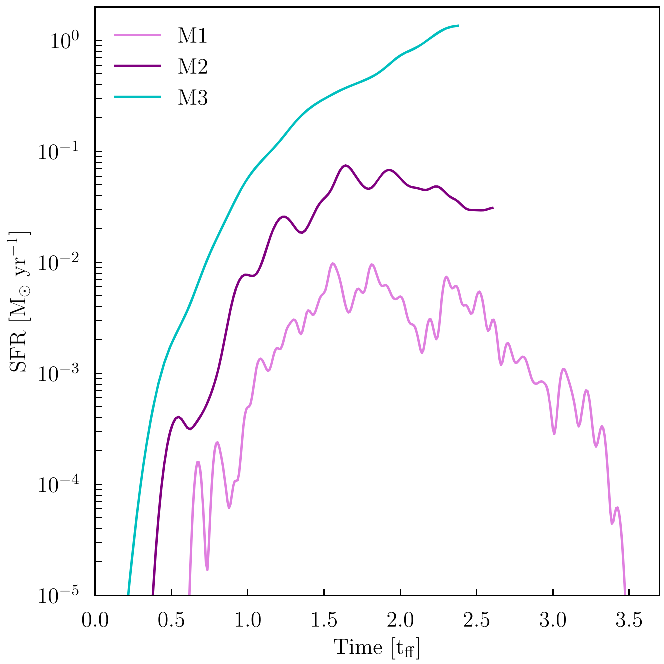

Figure 2. Star formation rate as a function of time in units of initial GMC freefall time. Note that all lines are slightly truncated at the end due to the Gaussian smoothing.

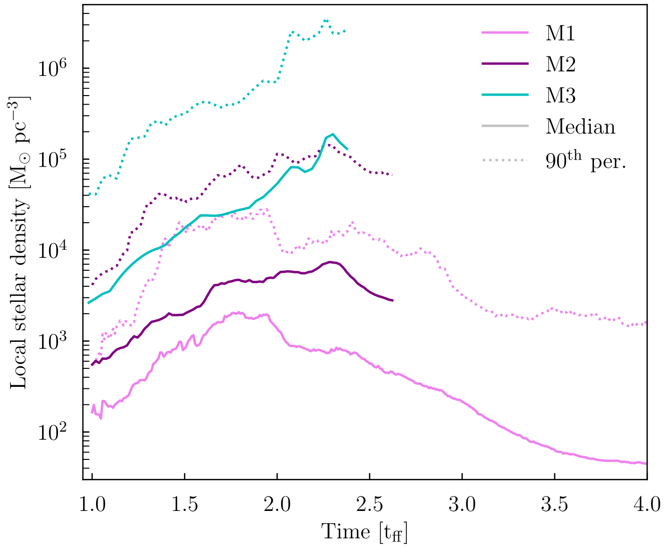

Figure 3. Median and 90th percentile local stellar density as a function of time in units of initial GMC freefall time.

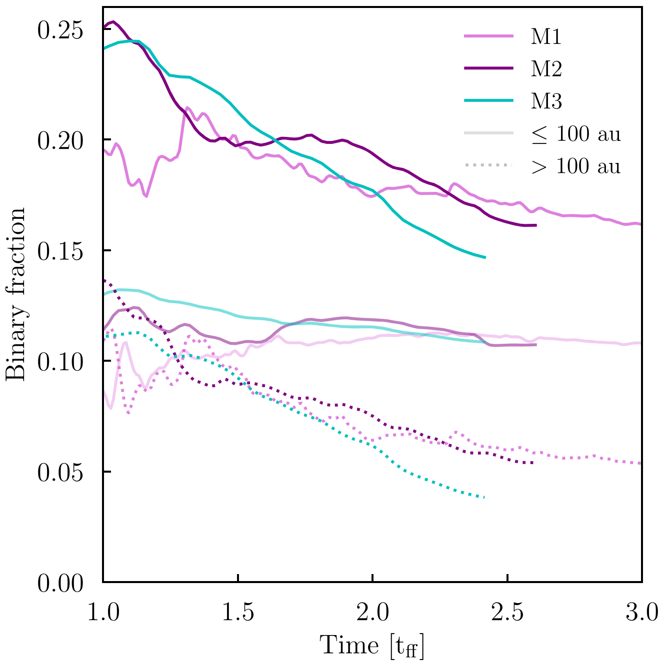

Figure 4. Binary fraction as a function of time in units of initial GMC freefall time. Binaries with close (⩽100 au) and wide (>100 au) companions are shown as faint solid and dotted curves. For comparison, a fully sampled binary population with the prescription used in this work has a binary fraction of 21%, with 12% of the stars having a close companion and 9% of the stars having a companion with an orbital separation above 100 au.

for M3 in the bottom row of Figure 5 (bottom left and bottom right). The primary masses generally shift toward larger values, while the mass ratios shift toward smaller values. The fraction of binaries with OB primaries (above 2 $M_\odot$) increases, with the strongest fractional increase seen for the most massive O-type stars. Lower-mass binaries often have lower binding energies, and are therefore more easily disrupted. On the other hand, massive single stars tend to easily acquire bound companions (as shown in J. E. Wall et al. 2019; C. Cournoyer-Cloutier et al. 2021). Two effects also contribute to the shift in mass ratios. First, dynamically formed systems, which make up about 5% of all binaries in this simulation, tend to be paired randomly and therefore favor smaller mass ratios, due to the shape of the IMF. Low-mass binaries, which make up most of the disrupted systems (see Section 4.4), tend to have mass ratios closer to unity; their disruption therefore shifts the distribution of mass ratios toward smaller values.

4.3. Dynamical Formation and Exchanges

We can also turn our attention to the relative contributions of primordial systems—which may be dynamically hardened or softened, or disrupted—and systems formed dynamically, either through exchanges or by capture. In Figure 6, we compare the semimajor axis distribution of binaries present in M3 after ∼2.5 $t_{\rm ff}$ (which are primordial at >95%) to those of the subset of dynamically formed binaries for all stars and for O-type stars only. For the full distribution, we find that dynamically formed binaries tend to be much wider than primordial binaries. On the other hand, for the subset of O stars, about half of the dynamically formed binaries (<5% of systems) have semimajor axes below 100 au; most of those are formed through exchanges. Despite their high binding energies, several primordial O-star binaries are also disrupted. Dynamical interactions during cluster formation therefore have an impact not only on the population of low-mass binaries, but also on the highest-mass systems. Although O stars have a constant binary fraction (see Figure 7), several O-star binaries are modified or disrupted.

4.4. The Influence of Environment

We now explicitly compare the evolution of the populations of binaries in the different environments. In Figure 7, we plot the binary fraction at ∼2.5 $t_{\rm ff}$ as a function of stellar mass for our simulations, compared to the primordial binaries. For M3 and M2, the binary fraction is lower than the primordial binary fraction for stellar masses <9 $M_\odot$, and is consistent within

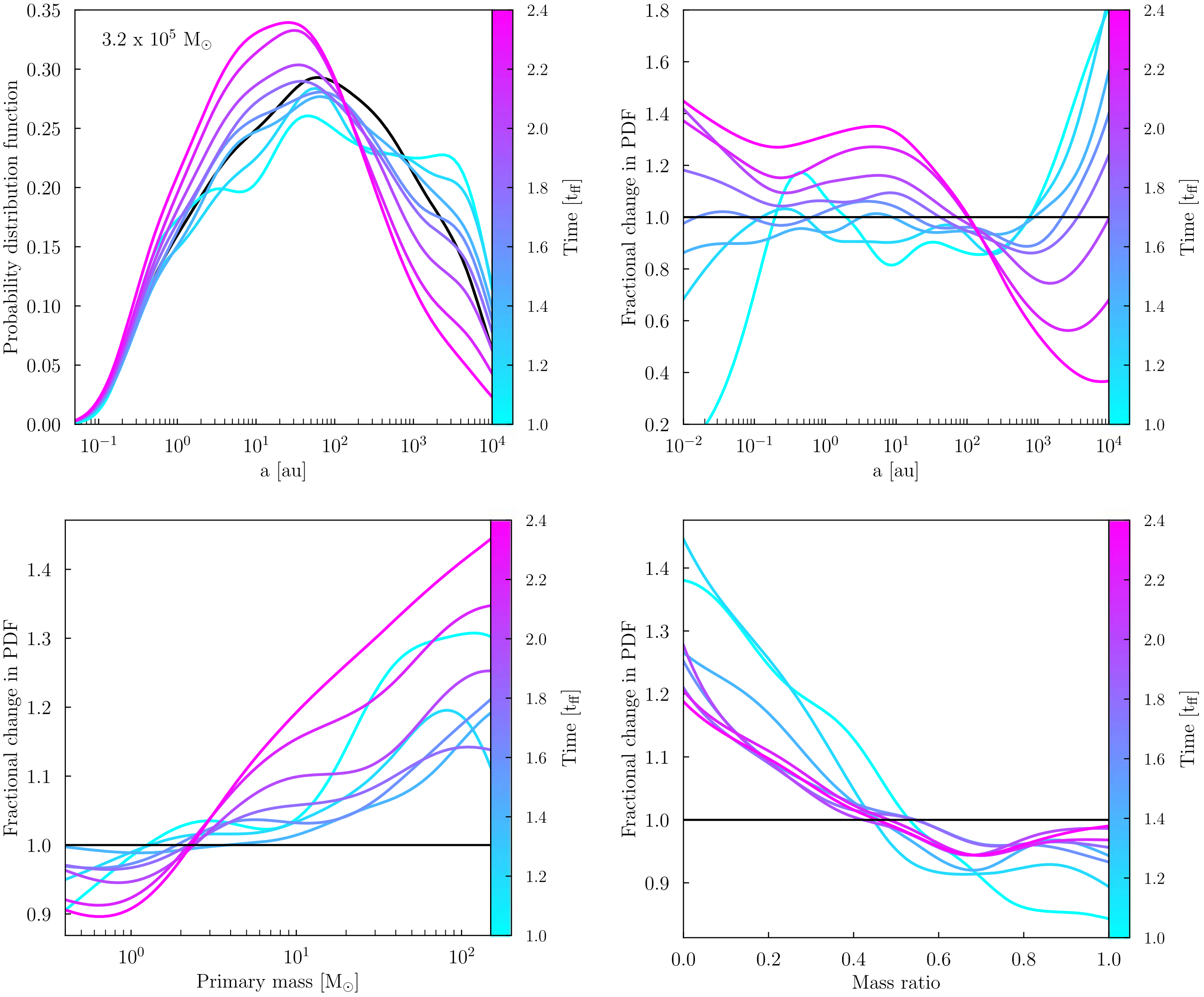

Figure 5. Top left: PDF of semimajor axes for M3, color coded as a function of time in units of freefall times of the initial cloud. The black line denotes the primordial distribution. Top right: the same, but normalized to the primordial distribution. Bottom left: PDF of primary masses, normalized to the primordial distribution (in black). Bottom right: PDF of mass ratios, normalized to the primordial distribution (in black).

uncertainties with the primordial binary fraction for stellar masses $\geqslant 9\,M_\odot$. A similar trend is found for the best estimate of the binary fraction for M1, although the binary fraction is always consistent within uncertainties with the primordial distribution due to the smaller number of stars formed. This indicates clearly that the binary fraction decreases during hierarchical cluster formation for lower-mass stars, while the binary fraction for massive stars is stable.

We also compare the PDF of semimajor axes to one another and to the primordial distribution at $\sim 2.5\,t_{\mathrm{ff}}$. We use the distribution of semimajor axes as evidence of the change in the binary population, as it is the metric that shows the clearest signature of change in one direction. For our statistical comparison, we use the two-sample Kolmogorov–Smirnov (KS) test. We are confident at >99% that all three distributions have smaller semimajor axes than the primordial distribution, and that M3 has smaller semimajor axes than M2 and M1. This confirms that similar trends in the evolution of populations of binaries emerge in different cluster-forming environments, and confirms that those trends are stronger in denser, more massive cluster-forming environments. We find that the distributions keep diverging from the primordial distribution of semimajor axes well after the change is reliably detected. This is most obvious for M3, for which the difference keeps increasing throughout the simulation. On the other hand, the distribution of semimajor axes becomes more stable for M1 at late times, following the binary fraction. Taken together with the results from Figures 2 and 4, this confirms that most of the changes in the binary fraction and binary orbital properties take place during cluster formation, while the star formation rate is high. We present a more detailed discussion of this time evolution in the Appendix.

5. Discussion

5.1. Comparison to Observations

We have simulated counterparts to cluster-forming regions with physical properties mimicking a large range of observed embedded clusters in the Local Group. Although the cluster-forming regions do not form a single, monolithic cluster within $2.5\,t_{\mathrm{ff}}$, we expect they will eventually form bound clusters of mass greater or equal to their current stellar mass.

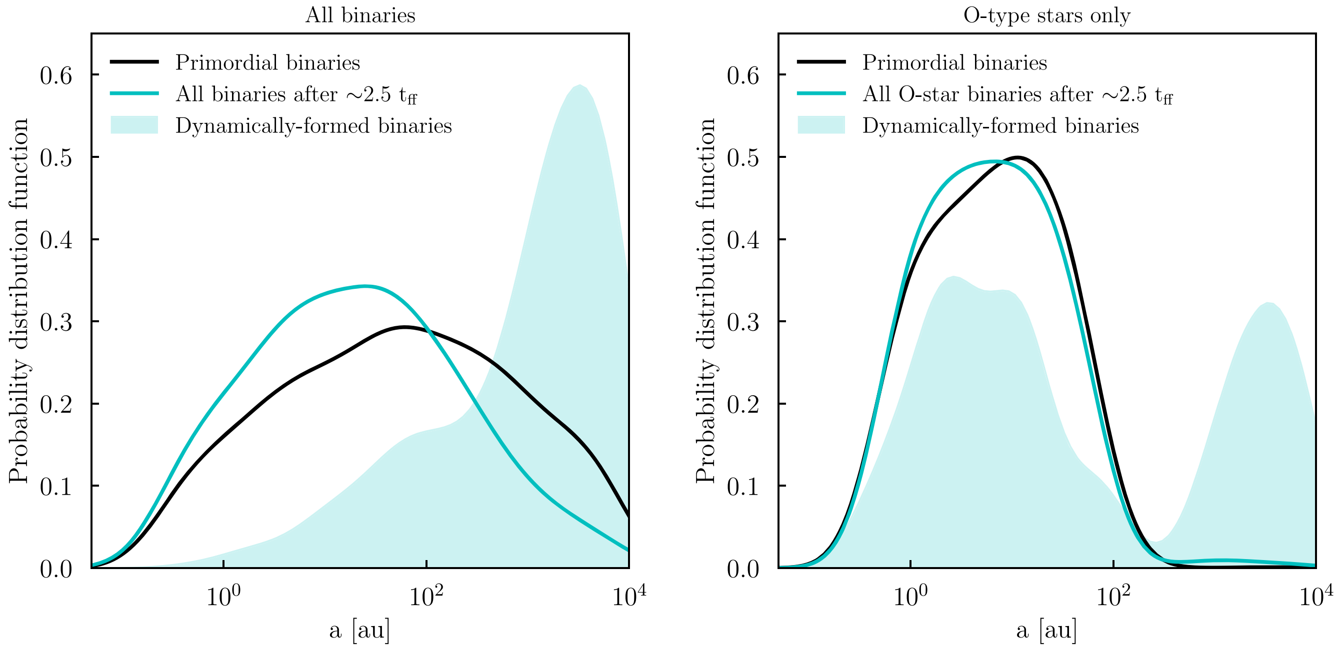

Figure 6. Left: semimajor of primordial binaries, all binaries present in cluster after 2.5 $t_{\rm ff}$, and dynamically formed binaries for M3. Right: the same, but for binaries with O-star primaries only.

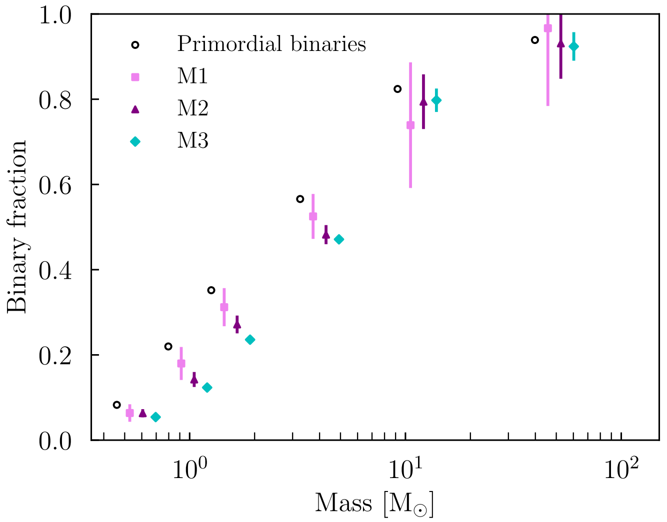

Figure 7. Left: binary fraction as a function of stellar mass after 2.5 $t_{\rm ff}$. The vertical lines correspond to the Poisson error, and the different runs are offset along the mass axis for readability. The mass bins used are the same ones as in Table 2, with the center of the mass bin at the midpoint between the M1 and M2 data points.

1. M1, which is evolved until gas expulsion, forms a total stellar mass of $7.8 \times 10^3\, M_\odot$, of which $6.9 \times 10^3\, M_\odot$ is bound. It can therefore be treated as a simulated counterpart to M16 (8100 stars), RCW 38 (9900 stars), or NGC 6357 (12,000 stars) (M. A. Kuhn et al. 2015), which are local embedded clusters hosting massive stars.
2. M2, which has formed roughly $3.4 \times 10^4\, M_\odot$ of stars (of which >99% are bound), is more similar to the Arches cluster, which has a stellar mass between 2×10^4 (P. Espinoza et al. 2009) and $\lesssim 7 \times 10^4$ (D. F. Figer et al. 2002), a density above $10^5\, M_\odot\,{\rm pc}^{-3}$ in its densest regions (P. Espinoza et al. 2009), and is known to have a high binary fraction for stars more massive than $50\, M_\odot$ (J. S. Clark et al. 2023).
3. M3, with a bound mass approaching $2 \times 10^5\, M_\odot$, is more massive than any YMC within the Milky Way (S. F. Portegies Zwart et al. 2010, and references therein), and about twice as massive as R136 in the LMC ($8.7 \times 10^4\, M_\odot$) (M. Cignoni et al. 2015), known to host several stars more massive than $100\, M_\odot$.

Our results confirm that a universal mass-dependent primordial binary fraction and distribution of orbital parameters naturally gives rise to variations in binary population properties with environment. Most of the changes in the properties of the binary population take place during the cluster assembly process, which is consistent with the decrease in binary fraction and the shift in binary properties being driven by subcluster mergers (as found in C. Cournoyer-Cloutier et al. 2024). This is important to take into account when comparing observations. Several clusters for which we have resolved observations show evidence of recent or ongoing mergers between subclusters (e.g., Westerlund 1, P. Zeidler et al. 2021; R136, E. Sabbi et al. 2012; K. Fahrion & G. De Marchi 2024). However, it is hard to constrain observationally whether a cluster has undergone a recent merger, even with resolved photometry for individual stars: signatures from the shape of the cluster are erased on very short timescales (C. Cournoyer-Cloutier et al. 2023), and signatures from an anisotropic distribution of runaway stars (B. Polak et al. 2024b) require high-quality observations away from the cluster center. The recent history of an embedded cluster therefore also likely contributes to setting its wide binary fraction and distribution of orbital properties, in addition to its density, therefore resolving the apparent inconsistency between the excess (H. Niu et al. 2020) or dearth (N. R. Deacon & A. L. Kraus 2020) of binaries observed in denser young open star clusters.

Our simulations reproduce the lower number of wide binaries for low- and solar-mass stars that are observed in dense star-forming regions (e.g., G. Duchêne et al. 2018), as well as the stable close binary fraction for clusters in the mass range of observed clusters in the Milky Way (N. R. Deacon &

A. L. Kraus 2020). For more massive clusters, however, our results suggest that the binary fraction for companions closer than 100 au also decreases during cluster assembly. Clouds with shorter freefall times—and therefore dense, compact clouds—show more rapid changes to their populations of binaries during cluster formation.

5.2. Implication for GC Formation

Although it is not possible to confirm observationally whether the most massive YMCs in starbursts in the local Universe are forming through subcluster mergers—let alone GCs at high redshift—there is strong evidence from simulations that the most massive star clusters assemble from the repeated mergers of smaller subclusters (C. S. Howard et al. 2018; C. L. Dobbs et al. 2022; S. Rieder et al. 2022; M. Reina-Campos et al. 2024). Observations in the local Universe and at high redshift both suggest that the most massive clusters should form from GMCs with high surface densities, and therefore, short freefall times: GMCs in local starburst galaxies have surface densities $\geqslant 10^3\,M_\odot\,\mathrm{pc}^{-2}$ (J. Sun et al. 2018), as do GMCs observed in a strongly lensed galaxy at $z \sim 1$ (M. Dessauges-Zavadsky et al. 2023). We therefore expect that clusters forming from those GMCs would exhibit similar behavior to that of our M3 model, in which the distribution of binaries is strongly modified at early times in the cluster formation process.

GCs tend to have low binary fractions ($\lesssim 10\%$ assuming a field-like mass ratio distribution) (A. P. Milone et al. 2012) for stars with masses $\lesssim 0.8\,M_\odot$. This corresponds to our lowest mass bin in Figure 7, and shows good agreement with our calculated fraction of systems with semimajor axes smaller than 10,000 au. If the primordial binary population is set by the physics of core and disk fragmentation—and therefore the same for cluster-forming environments of the same metallicity—then the hierarchical formation of massive clusters could be sufficient to explain the low binary fraction observed for low-mass stars in old GCs, while allowing for the high binary fraction for massive stars in YMCs.

In a recent paper, M. Nguyen & A. Sills (2024) showed that a population of massive binaries between 10 and $40\,M_\odot$, following the same distribution of orbital properties as our primordial distribution, loses about 25% of its initial mass as pre-supernova ejecta. This cool ejecta has the right abundances (as originally shown by S. E. de Mink et al. 2009) to explain the light abundance variations observed in the vast majority of GCs (known as multiple populations) (see N. Bastian & C. Lardo 2018; R. Gratton et al. 2019; A. P. Milone & A. F. Marino 2022, for recent reviews). In our simulations, the binary fraction for O-type stars shows very little change during the assembly process, even for the most massive, densest cloud. The semimajor axes, however, tend to shift to smaller values, and exchanges are ubiquitous, including for originally tight systems. This suggests that M. Nguyen & A. Sills (2024) may have underestimated the number of short-period systems present in a massive cluster, and therefore, the amount of cool, enriched ejecta. We also suggest that more massive clusters should host even more close binaries than M3, in agreement with the observations that show a stronger signal of enrichment in more massive clusters. As the close binary fraction of massive stars is insensitive to metallicity (M. Moe et al. 2019), the primordial binary properties for close, massive binaries should be similar for GCs forming at low metallicity and for massive stars observed in the local Universe. Our simulations thus indicate that GCs very likely hosted rich populations of close, massive binaries during their formation, supporting massive interacting binaries as a possible source of enriched material for multiple populations.

6. Conclusions

We have conducted simulations of YMC formation within GMCs with masses 2×10^4, 8×10^4, and $3.2 \times 10^5\,M_\odot$, and studied how populations of binary stars evolve during the cluster formation process. We have found that the binary fraction and the distribution of the binaries' orbital properties change faster and more strongly in more massive and denser clouds. This tendency is exacerbated by the nonlinear relationship between initial gas mass and final stellar density that we find. We summarize the key results below.

1. The binary fraction decreases rapidly in all our simulations while the SFR and the local stellar density are increasing. When the SFR and the local stellar density decrease, the binary fraction stabilizes.
2. A similar trend is found for the changes in the distributions of orbital properties, due to a combination of binary disruption, exchanges, and dynamical binary formation, along with ongoing star formation. The clearest trends with time are seen for the semimajor axis, which shifts toward smaller values throughout the cluster assembly process.
3. The decrease in the binary fraction is driven by a decrease in the wide (>100 au) binary fraction, although the most massive, densest cluster-forming region also shows a decrease in its close binary fraction.
4. For the most massive, densest cluster-forming region, the distribution of semimajor axes becomes measurably different from the primordial distribution after about $1.5\,t_{\mathrm{ff}}$, despite the ongoing rapid star formation after this point. On the other hand, for lower-density environments, the distribution takes a longer time to become measurably different from the primordial distribution, due to the less concentrated star formation.
5. The binary fraction does not change for O-type stars, and the distribution of O stars only shows a small shift toward smaller semimajor axes. Individual systems, including ones with very tight orbits, can however be modified, for example, via exchanges with other systems.

We have found that populations of binaries evolve during clustered star formation within GMCs, and that a universal field-like primordial distribution can naturally explain the observed trends with cluster mass and density for Galactic clusters. Changes are more rapid and stronger in more massive, denser GMCs, which can naturally explain the differences in binary fractions and binary orbital properties observed in different clustered environments. While the present paper investigates the evolution of the population of binaries during star cluster formation, binaries may also impact their host cluster. In future papers in this series, we will investigate runaway stars and stellar mergers in clusters with realistic populations of binaries, as well as the effects of binary stellar evolution on star formation within cluster-forming regions (C. Cournoyer-Cloutier et al. 2024, in preparation).

Acknowledgments

C.C.C. is supported by a Canada Graduate Scholarship—Doctoral (CGS D) from the Natural Sciences and Engineering Research Council of Canada (NSERC). A.S. and W.E.H. are supported by NSERC. This research was enabled in part by support provided by Compute Ontario (https://www.computeontario.ca/) and the Digital Research Alliance of Canada (alliancecan.ca) via the research allocation FT #2665: The Formation of Star Clusters in a Galactic Context. Some of the code development that facilitated this study was done on Snellius through the Dutch National Supercomputing Center SURF grant 15220. M.-M.M.L, B.P., and E.A. were partly supported by NSF grant AST23-07950. E.A. was partly supported by NASA grant 80NSSC24K0935. S.M.A. is supported by an NSF Astronomy and Astrophysics Postdoctoral Fellowship, which is supported by the National Science Foundation under award No. AST24-01740; S.M.A. also received support from award No. AST20-09679.

Appendix
Statistical Test of Semimajor Axis Evolution

We compare the distribution of semimajor axes in all of our simulations, at every snapshot, to the primordial distribution. We do so to investigate at what time changes to the population of binaries can be reliably measured in different environments, and whether the population continues to evolve beyond this point. In Figure 8, we plot the probability, as a function of time, that the distribution of semimajor axes has shifted toward smaller values compared to the sampled distribution. The probability is calculated from the KS test, as 1-*p*. The probability obtained from the KS test, however, only answers the question of whether the semimajor axes are smaller than in the primordial distribution, but does not measure by how much the distributions differ. The KS statistic itself, however, provides a measure of the difference between the two distributions. We also plot it as a function of time in Figure 8. In all cases, we compare the distribution of binaries present within a cluster-forming region to the primordial distribution. We emphasize that the primordial distribution is not an initial distribution, but rather the distribution for newly formed binaries; at any given time, the observed binary population arises from the combined contributions of primordial binary formation and the effects of dynamics.

At early times, both the probability and the KS statistic are nonzero in all simulations, due to the small number of stars formed. They approach zero around $\sim 1.5\, t_{\rm ff}$, when the combination of stellar dynamics and new star formation result in a binary population that is very similar to the primordial population. This effect is strongest for M1, which has the fewest stars. At later times, the effects of stellar dynamics start to dominate over the formation of primordial binaries, and changes in the binary population become detectable.

For all three clusters, the probability stabilizes at >99%. It reaches this value earlier for M3 than for M2, and earlier for M2 than for M1. Changes in massive cluster-forming clouds are stronger, and happen more quickly than in lower-mass clouds. We also note that the lower-mass models, in particular M1, can oscillate strongly between subsequent checkpoints, due to bursts in star formation. The same effect can be seen, albeit more weakly, in M2. M3, on the other hand, goes almost directly to a probability of 100% and remains there, despite the high star (and therefore primordial binary) formation rate. We can calculate a time τ_c, after which the probability is stable at >99%, i.e., a timescale for a significant change in the binary population, for all simulations. We get values of 2.37, 1.98, and 1.66 $t_{\rm ff}$ (2.51, 1.05, and 0.44 Myr) for M1, M2, and M3. We find that the timescale for change increases with the cloud's initial freefall time. τ_c increases superlinearly with freefall time, like the stellar mass formed in the clouds: more massive, denser clouds undergo more rapid star formation and more rapid changes to their populations of binaries.

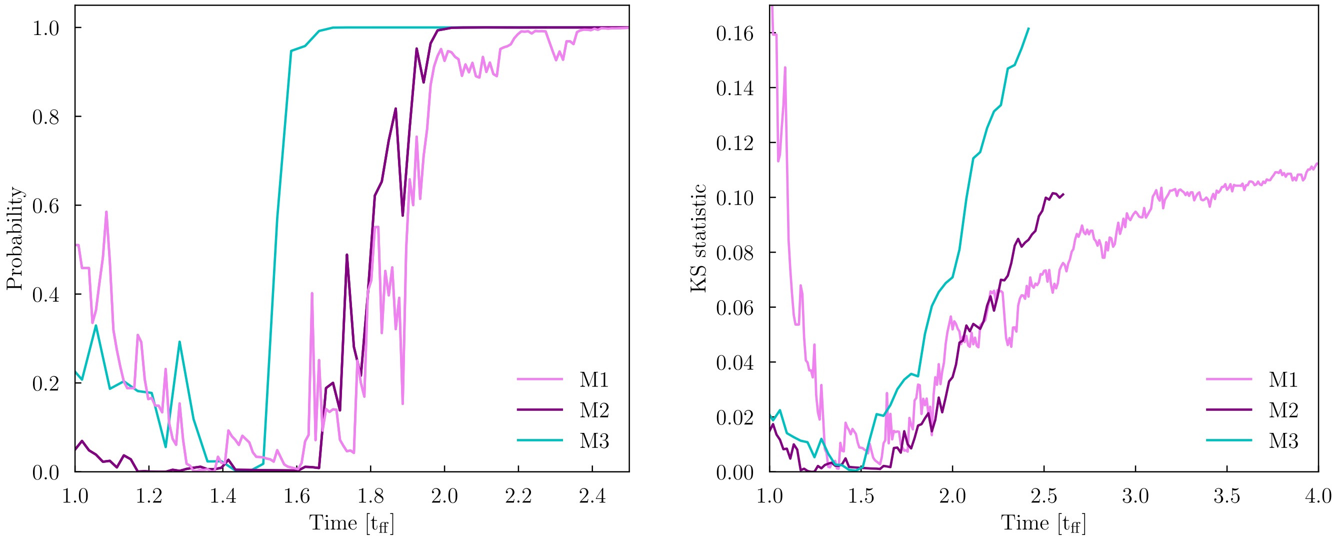

Figure 8. Left: probability that the semimajor axes are smaller than in the primordial distribution as a function of time. M1, M2, and M3 consistently show a difference relative to the primordial distribution after 2.37, 1.98, and 1.66 $t_{\rm ff}$ (2.51, 1.05, and 0.44 Myr). Right: KS statistic measuring the amount of change from the primordial distribution as a function of time.

ORCID iDs

Claude Cournoyer-Cloutier https://orcid.org/0000-0002-6116-1014
Alison Sills https://orcid.org/0000-0003-3551-5090
William E. Harris https://orcid.org/0000-0001-8762-5772
Brooke Polak https://orcid.org/0000-0001-5972-137X
Steven Rieder https://orcid.org/0000-0003-3688-5798
Eric P. Andersson https://orcid.org/0000-0003-3479-4606
Sabrina M. Appel https://orcid.org/0000-0002-6593-3800
Mordecai-Mark Mac Low https://orcid.org/0000-0003-0064-4060
Stephen McMillan https://orcid.org/0000-0001-9104-9675
Simon Portegies Zwart https://orcid.org/0000-0001-5839-0302

References

Adamo, A., Bradley, L. D., Vanzella, E., et al. 2024, Natur, 632, 513
Adamo, A., Usher, C., Pfeffer, J., & Claeyssens, A. 2023, MNRAS, 525, L6
Andersson, E. P., Agertz, O., & Renaud, F. 2020, MNRAS, 494, 3328
Andersson, E. P., Agertz, O., Renaud, F., & Teyssier, R. 2023, MNRAS, 521, 2196
Baczynski, C., Glover, S. C. O., & Klessen, R. S. 2015, MNRAS, 454, 380
Barnes, J., & Hut, P. 1986, Natur, 324, 446
Bastian, N., & Lardo, C. 2018, ARA&A, 56, 83
Blaauw, A. 1961, BAN, 15, 265
Chen, B.-Q., Li, G.-X., Yuan, H.-B., et al. 2020, MNRAS, 493, 351
Cignoni, M., Sabbi, E., van der Marel, R. P., et al. 2015, ApJ, 811, 76
Claeyssens, A., Adamo, A., Richard, J., et al. 2023, MNRAS, 520, 2180
Clark, J. S., Lohr, M. E., Najarro, F., Patrick, L. R., & Ritchie, B. W. 2023, MNRAS, 521, 4473
Colella, P., & Woodward, P. R. 1984, JCoPh, 54, 174
Cournoyer-Cloutier, C., Karam, J., Sills, A., Portegies Zwart, S., & Wilhelm, M. 2024, ApJ, 975, 207
Cournoyer-Cloutier, C., Sills, A., Harris, W. E., et al. 2023, MNRAS, 521, 1338
Cournoyer-Cloutier, C., Tran, A., Lewis, S., et al. 2021, MNRAS, 501, 4464
de Mink, S. E., Pols, O. R., Langer, N., & Izzard, R. G. 2009, A&A, 507, L1
Deacon, N. R., & Kraus, A. L. 2020, MNRAS, 496, 5176
Dessauges-Zavadsky, M., Richard, J., Combes, F., et al. 2023, MNRAS, 519, 6222
Dobbs, C. L., Bending, T. J. R., Pettitt, A. R., & Bate, M. R. 2022, MNRAS, 509, 954
Dubey, A., Antypas, K., Calder, A. C., et al. 2014, Int. J. High Perform. Comput. Appl., 28, 225
Duchêne, G., Lacour, S., Moraux, E., Goodwin, S., & Bouvier, J. 2018, MNRAS, 478, 1825
Espinoza, P., Selman, F. J., & Melnick, J. 2009, A&A, 501, 563
Fahrion, K., & De Marchi, G. 2024, A&A, 681, A20
Faisst, A. L., Chary, R. R., Brammer, G., & Toft, S. 2022, ApJL, 941, L11
Federrath, C., Banerjee, R., Clark, P. C., & Klessen, R. S. 2010, ApJ, 713, 269
Figer, D. F., Najarro, F., Gilmore, D., et al. 2002, ApJ, 581, 258
Fryxell, B., Olson, K., Ricker, P., et al. 2000, ApJS, 131, 273
Fujii, M., Iwasawa, M., Funato, Y., & Makino, J. 2007, PASJ, 59, 1095
Götberg, Y., de Mink, S. E., Groh, J. H., et al. 2018, A&A, 615, A78
Gratton, R., Bragaglia, A., Carretta, E., et al. 2019, A&ARv, 27, 8
Guszejnov, D., Markey, C., Offner, S. S. R., et al. 2022, MNRAS, 515, 167
Harris, W. E., & Reina-Campos, M. 2023, MNRAS, 526, 2696
He, H., Wilson, C., Brunetti, N., et al. 2022, ApJ, 928, 57
Heitsch, F., Mac Low, M.-M., & Klessen, R. S. 2001, ApJ, 547, 280
Howard, C. S., Pudritz, R. E., & Harris, W. E. 2018, NatAs, 2, 725
Iwasawa, M., Tanikawa, A., Hosono, N., et al. 2016, PASJ, 68, 54
Jerabkova, T., Beccari, G., Boffin, H. M. J., et al. 2019, A&A, 627, A57
Joncour, I., Duchêne, G., & Moraux, E. 2017, A&A, 599, A14
Kalari, V. M., Vink, J. S., de Wit, W. J., Bastian, N. J., & Méndez, R. A. 2019, A&A, 625, L2
Karam, J., & Sills, A. 2024, ApJ, 967, 86
Kounkel, M., Covey, K., Moe, M., et al. 2019, AJ, 157, 196
Kraus, A. L., Ireland, M. J., Martinache, F., & Hillenbrand, L. A. 2011, ApJ, 731, 8
Kroupa, P. 2002, Sci, 295, 82
Kuhn, M. A., Getman, K. V., & Feigelson, E. D. 2015, ApJ, 802, 60
Lahén, N., Naab, T., Johansson, P. H., et al. 2020, ApJ, 904, 71
Lancaster, L., Ostriker, E. C., Kim, J.-G., & Kim, C.-G. 2021, ApJL, 922, L3
Lee, M. G., Bae, J. H., & Jang, I. S. 2022, ApJL, 940, L19
Lohner, R. 1987, CMAME, 61, 323
MacNeice, P., Olson, K. M., Mobarry, C., de Fainchtein, R., & Packer, C. 2000, CoPhC, 126, 330
Makino, J., & Aarseth, S. J. 1992, PASJ, 44, 141
Menon, S. H., Federrath, C., & Krumholz, M. R. 2023, MNRAS, 521, 5160
Miholics, M., Kruijssen, J. M. D., & Sills, A. 2017, MNRAS, 470, 1421
Milone, A. P., & Marino, A. F. 2022, Univ, 8, 359
Milone, A. P., Piotto, G., Bedin, L. R., et al. 2012, A&A, 540, A16
Miyoshi, T., & Kusano, K. 2005, JCoPh, 208, 315
Moe, M., & Di Stefano, R. 2017, ApJS, 230, 15
Moe, M., Kratter, K. M., & Badenes, C. 2019, ApJ, 875, 61
Nguyen, M., & Sills, A. 2024, ApJ, 969, 18
Niu, H., Wang, J., & Fu, J. 2020, ApJ, 903, 93
Offner, S. S. R., Moe, M., Kratter, K. M., et al. 2023, in ASP Conf. Ser. 534, Protostars and Planets VII, ed. S. Inutsuka et al. (San Francisco, CA: ASP), 275
Pelupessy, F. I., van Elteren, A., de Vries, N., et al. 2013, A&A, 557, A84
Polak, B., Mac Low, M.-M., Klessen, R. S., et al. 2024a, A&A, 690, A94
Polak, B., Mac Low, M.-M., Klessen, R. S., et al. 2024b, A&A, 690, A207
Portegies Zwart, S., McMillan, S., Harfst, S., et al. 2009, NewA, 14, 369
Portegies Zwart, S., & McMillan, S. L. W. 2019, Astrophysical Recipes: The Art of Amuse (Bristol: IOP Publishing)
Portegies Zwart, S. F., McMillan, S. L. W., & Gieles, M. 2010, ARA&A, 48, 431
Portegies Zwart, S. F., McMillan, S. L. W., van Elteren, A., Pelupessy, F. I., & de Vries, N. 2013, CoPhC, 184, 456
Poveda, A., Ruiz, J., & Allen, C. 1967, BOTT, 4, 86
Reina-Campos, M., Gnedin, O. Y., Sills, A., & Li, H. 2024, arXiv:2408.04694
Ricker, P. M. 2008, ApJS, 176, 293
Rieder, S., Dobbs, C., Bending, T., Liow, K. Y., & Wurster, J. 2022, MNRAS, 509, 6155
Roman-Duval, J., Jackson, J. M., Heyer, M., Rathborne, J., & Simon, R. 2010, ApJ, 723, 492
Sabbi, E., Lennon, D. J., Gieles, M., et al. 2012, ApJL, 754, L37
Sana, H., de Mink, S. E., de Koter, A., et al. 2012, Sci, 337, 444
Steinwandel, U. P., Bryan, G. L., Somerville, R. S., Hayward, C. C., & Burkhart, B. 2023, MNRAS, 526, 1408
Stoop, M., Derkink, A., Kaper, L., et al. 2024, A&A, 681, A21
Stoop, M., Kaper, L., de Koter, A., et al. 2023, A&A, 670, A108
Sun, J., He, H., Batschkun, K., et al. 2024, ApJ, 967, 133
Sun, J., Leroy, A. K., Rosolowsky, E., et al. 2022, AJ, 164, 43
Sun, J., Leroy, A. K., Schinnerer, E., et al. 2020, ApJL, 901, L8
Sun, J., Leroy, A. K., Schruba, A., et al. 2018, ApJ, 860, 172
Vanzella, E., Claeyssens, A., Welch, B., et al. 2023, ApJ, 945, 53
Wall, J. E., Mac Low, M.-M., McMillan, S. L. W., et al. 2020, ApJ, 904, 192
Wall, J. E., McMillan, S. L. W., Mac Low, M.-M., Klessen, R. S., & Portegies Zwart, S. 2019, ApJ, 887, 62
Wang, L., Iwasawa, M., Nitadori, K., & Makino, J. 2020a, MNRAS, 497, 536
Wang, L., Nitadori, K., & Makino, J. 2020b, MNRAS, 493, 3398
Winters, J. G., Henry, T. J., Jao, W.-C., et al. 2019, AJ, 157, 216
Zapartas, E., de Mink, S. E., Izzard, R. G., et al. 2017, A&A, 601, A29
Zeidler, P., Sabbi, E., Nota, A., & McLeod, A. F. 2021, AJ, 161, 140